

State-dependence of polar amplification in an idealized, ice-free GCM

Andrew I. L. Williams^{1*} and Timothy M. Merlis¹

¹Program in Atmospheric and Oceanic Sciences, Princeton University, Princeton, NJ

Key Points:

- Polar amplification (PA) is simulated in a wide range of climate states using an idealized moist atmospheric general circulation model.
- Ice-free climates with warmer global-mean surface temperature and/or stronger meridional temperature gradients have more PA.
- Atmospheric energy transport is the dominant factor underlying PA's state-dependence, with a smaller contribution from radiative processes.

*300 Forrestal Rd., Princeton, NJ 08528

Corresponding author: Andrew Williams, andrew.williams@princeton.edu

Abstract

Polar amplification (PA) is a robust feature of contemporary climate change, but its state-dependence across different climate conditions remains poorly understood despite potential relevance to paleoclimate records and future projections. Here we examine the state-dependence of PA across a wide range of climate states in an idealized moist general circulation model (GCM), without sea-ice. We generate a phase space of climate states with different global-mean surface temperature and equator-to-pole surface temperature contrast, and perturb each with longwave radiative forcing. We find that PA is larger in climates with higher global-mean surface temperatures and stronger meridional surface temperature gradients, consistent with moist energy balance model theory. We decompose the simulated PA into contributions from atmospheric energy transport, radiative forcing, and radiative feedbacks and find the state-dependence of PA in our experiments primarily arises through that of atmospheric energy transport. This has implications for both past and future ice-free climate states.

Plain Language Summary

Polar regions experience rapid climate change from human activities, a longstanding feature of Arctic climate change simulations. Idealized climate modeling approaches have revealed that large-scale atmospheric motion plays an important role in influencing temperature change at high latitudes. These large-scale atmospheric transports depend on the global-mean surface temperature and the equator-to-pole temperature contrast. Here, we examine how polar amplification of surface temperature change depends on the background climate state using idealized climate model simulations across climate states that vary substantially in these two key characteristics. The state-dependence of polar amplification in these simulations shows that changes in atmospheric energy transport are key, with a more modest role from local changes in radiative processes.

1 Introduction

The pattern of surface temperature change in response to radiative forcing often has a polar-amplified pattern, with more warming at high latitudes than low latitudes. Multiple mechanisms can give rise to polar amplification (PA) under warming, including the effects of sea ice loss, increased atmospheric energy transport, and a locally destabilizing atmospheric lapse rate feedback (as reviewed by Taylor et al., 2022). Extensive analysis of PA exists in comprehensive climate model projections of future climate (e.g., Winton, 2006; Hwang et al., 2011; Hahn et al., 2021), and it appears in both cold paleoclimate states, like the Last Glacial Maximum (Masson-Delmotte et al., 2006), and hot paleoclimate states, like the Eocene (Huber & Caballero, 2011; Henry & Vallis, 2022). The ubiquity of PA across vastly different climate states raises fundamental questions about whether the magnitude and mechanisms of PA depend on the base climate state itself. Understanding such state-dependence is useful for interpreting paleoclimate records and assessing how PA might evolve as the climate warms.

A common theoretical tool for studying the pattern of surface temperature change is one-dimensional, diffusive moist energy balance models (MEBMs). MEBMs can emulate the results of comprehensive GCM simulations given prescribed spatially varying radiative forcing, radiative feedback, and ocean heat uptake (Bonan et al., 2018; Hill et al., 2022). MEBMs exhibit PA, even with with spatially uniform radiative forcing and feedbacks (Flannery, 1984), because of an increase in latent energy transport with warming (partially offset by local radiative restoring and a decrease in dry energy transport). Furthermore, analytic solutions exist for this moist EBM configuration (Merlis & Henry, 2018) which predict that PA should be state-dependent, with larger PA when the base state has warmer global-mean surface temperature and/or stronger meridional temperature gradients. The MEBM’s state-dependence arises because of the well-established

state-dependence of latent energy transport changes (e.g., Caballero & Langen, 2005; O’Gorman & Schneider, 2008a; Kaspi & Showman, 2015; Guendelman & Kaspi, 2020; Merlis et al., 2022; Hahn et al., 2023).

While MEBMs are valuable for examining state-dependence of PA, they clearly omit important processes. In particular, the absence of vertical structure of the atmospheric response is a limitation. (Note that this is implicitly included when GCM-derived lapse rate feedback is prescribed.) Therefore, it is worth moving to the next ‘rung’ in climate model hierarchy (Held et al., 2005; Jeevanjee et al., 2017; Maher et al., 2019) and examining whether the expectations of this theory bear out. To do this, we examine the state-dependence of PA in a series of idealized moist GCM simulations. The simulations allow for spatially varying, state-dependent temperature feedbacks. They also allow for a climate-state-dependent diffusivity of the atmospheric macroturbulence, a factor typically neglected in MEBMs, though it can be included (Chang & Merlis, 2023). Given that these GCM simulations break assumptions of the simplest MEBM theory, it is worthwhile to examine whether the aggregate effect of these other degrees of freedom alters the overall state-dependence of PA. Our focus on state-dependence of PA extends previous work which has used idealized GCM simulations to shed light on the role of atmospheric processes in driving contemporary PA (e.g., Langen et al., 2012; Henry & Merlis, 2019; Feldl & Merlis, 2021; Merlis et al., 2022; Lu et al., 2022).

We focus on GCM simulations without a representation of sea-ice for three reasons: to better compare with the analytical MEBM theory, which neglects sea-ice; because systematically generating a phase space of climate states would be more difficult if sea-ice were included; and because the study of ‘ice-free PA’ is helpful for understanding PA in climates with perpetual ice-free conditions such as the early Eocene (Henry & Vallis, 2022). However, sea-ice processes are clearly of first-order importance for PA and its state-dependence in Earth-like climates, so we view this study only as a first step towards understanding the full state-dependence of PA.

We proceed as follows: In the next section, we present the idealized GCM model configuration and the results of the series of simulations where the base-state global-mean surface temperature and equator-to-pole meridional surface temperature contrast are varied. We then present an analysis of the local surface energy budget, expressed as a surface warming. The conclusion discusses different ways of combining the local energy budget components and the role of omitted processes in the idealized GCM.

2 Idealized GCM

2.1 Overview

The idealized aquaplanet GCM used in this work is a configuration of Isca (Vallis et al., 2018) that follows closely Frierson et al. (2006) and O’Gorman and Schneider (2008b). The representation of physical processes in the atmosphere is idealized in several ways. The radiation is represented by a gray scheme (no cloud or water vapor radiative effects) and the ‘microphysics’ is a saturation adjustment to 100% relative humidity using an idealized formulation of the Clausius–Clapeyron relation with the condensed water assumed to instantaneously fall to the surface as precipitation (i.e., there are no condensed water phases in the atmosphere). We also only consider vapor–liquid phase change (i.e. there is no ice in the model). A simplified Betts-Miller scheme relaxes convectively unstable profiles toward a moist adiabat with a 2-hour timescale (Frierson, 2007). The insolation is a time-independent distribution that approximates a perpetual annual-mean using a second Legendre polynomial specification and there is no atmospheric absorption of solar radiation. To perturb the climate, the longwave optical depth is increased by 40%, following Henry and Merlis (2019).

The lower boundary condition is a slab ocean with an albedo of 0.22—much higher than the albedo of water to compensate for the absence of atmospheric reflection. The heat capacity of 20 m of water allows for rapid equilibration. All simulations are performed at T42 spectral truncation ($\approx 2.8^\circ$ horizontal resolution) with 50 vertical levels in the model’s sigma (pressure divided by surface pressure) coordinate and are integrated for 3000 days. The analysis is conducted over the final 1500 days once the simulations have reached steady-state. A prescribed ocean energy source/sink term allows us to generate a wide range of climate base states, which is described next.

We use a gray radiation scheme—as opposed to Isca’s correlated-k radiation scheme, RRTMG (Mlawer et al., 1997)—to prevent errors associated with out-of-bounds usage of RRTMG (Kluft et al., 2019) when we explore more extreme climate states. Another approach would be to use a radiation scheme which is validated at these extreme temperatures, e.g., the SOCRATES scheme (Manners et al., 2017). However, using a gray radiation scheme greatly simplifies the calculation of radiative feedbacks compared to a more comprehensive scheme like SOCRATES, in addition to minimizing the computational expense.

2.2 Generating a Wide Range of Base States

The use of slab ocean boundary conditions is critical to allow the perturbed climates to develop an energetically consistent pattern of surface temperature change. Therefore, we need a systematic method for generating control climates with different global-mean and temperature gradients. To do so, we first perform simulations with prescribed sea surface temperature (SST) and use the equilibrated surface energy budget to determine the Q-flux that would generate that climate in a slab ocean simulation. The fixed-SST simulations are run for 1500 days, with analysis conducted over the final 200 days. Typically, a Q-flux represents the divergence of the vertically integrated ocean energy transport, which would have zero global-mean. Here, the Q-flux can be a global-mean surface energy source or sink.

Simulations with prescribed sea surface temperature (SST) are performed using the following idealized function:

$$\text{SST}(\phi) = T_0 + \frac{\Delta_h}{2} [3 \sin^2(\phi) - 1], \quad (1)$$

with global-mean SST, T_0 , and the equator-to-pole contrast controlled by the parameter, Δ_h , that multiplies the second Legendre polynomial. The imbalance between the net turbulent surface fluxes F_s and the net surface radiation R_s determines the Q-flux Q . In other words, the equilibrium surface energy budget of these prescribed SST simulations is $Q = F_s + R_s$. This Q can then be prescribed in a slab ocean boundary condition to reproduce the SST given by (1). The slab ocean model is then perturbed with the increased longwave optical depth to examine how the pattern of the forced response of surface temperature varies with the control surface temperature distribution. In total, 77 base climates are simulated: the global-mean surface temperature spans 270 to 300 K and the equator-to-pole contrast spans 15 to 135 K. Each is paired with an increased longwave optical depth warmed simulation.

The prescribed SST simulations that determine the Q-flux are also used to calculate the radiative forcing for each climate. An effective radiative forcing (also known as troposphere-adjusted forcing) calculation involves differencing the top-of-atmosphere net radiation in a simulation with unchanged SST and increased optical depth from the control.

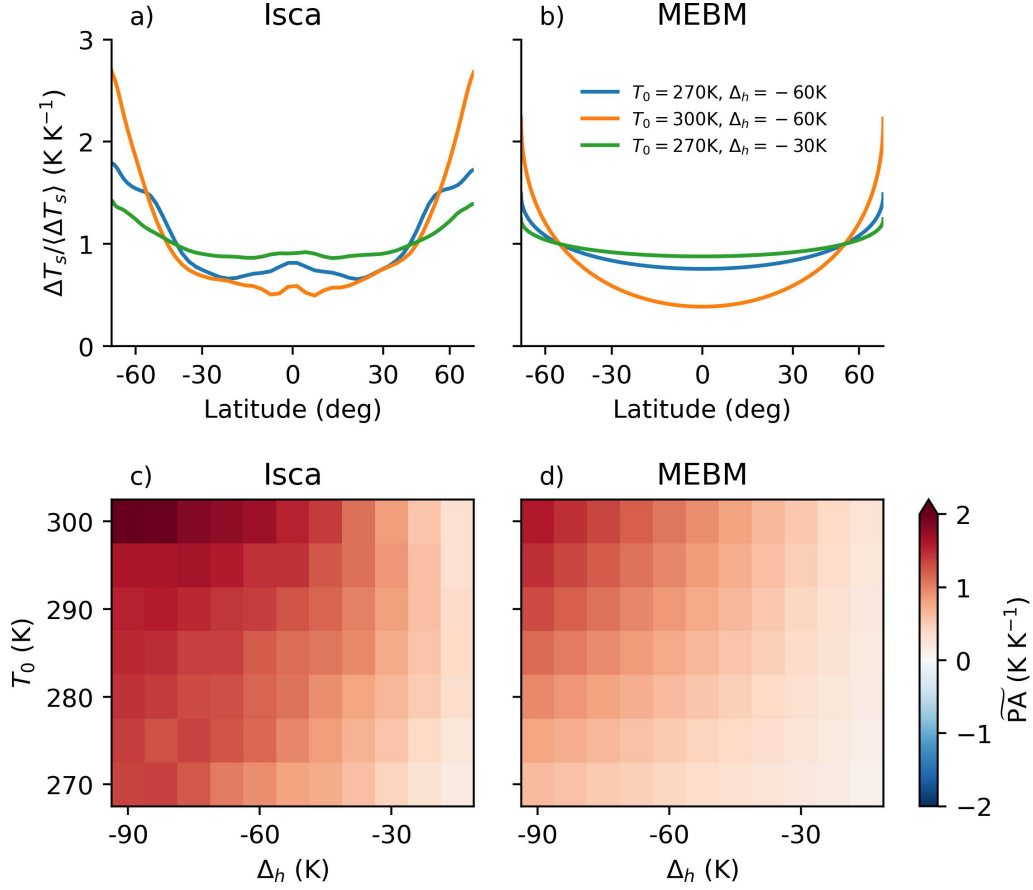


Figure 1. (Top row) Pattern of surface temperature change for three base climate states as (a) simulated by an idealized, ice-free GCM and (b) calculated via moist EBM theory (Eq. 3). (Bottom row) The state-dependence of a PA metric (Eq. 2) for a wide range of base climate states, where the global-mean surface temperature (vertical axis) and equator-to-pole surface temperature contrast (horizontal axis) are varied for (c) idealized GCM simulations and (d) moist EBM theory. All temperature change patterns and metrics are normalized by the global-mean surface temperature change, and hence have units of K K^{-1} .

3 Simulated state-dependence of PA

3.1 Idealized GCM Results

Figure 1a shows the change in surface temperature in response to increased optical depth for three climate states: an Earth-like one, one that has a uniform global increase in surface temperature, and one that has a decreased meridional temperature contrast with unchanged global-mean surface temperature. The Earth-like base climate has approximately twice as much warming at the pole than in the global mean (Fig. 1a, blue line), while the simulation with a warmer mean state has about 2.5 times as much warming at the pole than in the global mean and the simulation with stronger meridional temperature gradients has enhanced polar warming by about a factor of 2.2.

To illustrate the PA state-dependence over the full range of simulations, we define a PA metric, $\widetilde{\text{PA}}$. This metric is the difference between a polar cap and tropical aver-

age, normalized by the global-mean surface temperature:

$$\widetilde{\text{PA}} \equiv \frac{\Delta T_s|_{pole}}{\langle \Delta T_s \rangle} - \frac{\Delta T_s|_{trop}}{\langle \Delta T_s \rangle}, \quad (2)$$

with the polar cap bounded by 60° and the tropical average taken within 30° of the equator. The appeal of normalizing by the global-mean surface temperature change is that there is some state-dependence in this model’s climate sensitivity: it varies from ≈ 4 to ≈ 6 K for this change in optical depth. Eliminating this climate sensitivity variation isolates the pattern of warming.

Figure 1c shows $\widetilde{\text{PA}}$ over the range of climates with varied global-mean surface temperature (vertical axis) and varied equator-to-pole surface temperature contrast (horizontal axis). Stronger PA with warmer base climate states and/or with greater meridional temperature gradients is a systematic feature of these GCM simulations.

3.2 Comparison to Moist EBM Theory

Moist EBM theory for PA uses a spectral expansion of the EBM’s governing equation and truncates at the second Legendre polynomial (Merlis & Henry, 2018; Chang & Merlis, 2023). The sensitivity of the second Legendre polynomial component of temperature T_2 , which controls the equator-to-pole temperature contrast, with respect to global-mean surface temperature T_0 depends on climatological—indicated by $\overline{(\cdot)}$ —temperature gradients, moist thermodynamic properties, and global-mean radiative feedback parameter λ_0 :

$$\frac{\partial T_2}{\partial T_0} = \frac{-6\overline{\mathcal{D}}\overline{T_2}L\overline{\mathcal{H}_0}c_p^{-1}\partial_{TT}q^*|_{\overline{T_0}}}{6\overline{\mathcal{D}}(1 + L\overline{\mathcal{H}_0}c_p^{-1}\partial_T q^*|_{\overline{T_0}}) - \lambda_0}, \quad (3)$$

with diffusivity \mathcal{D} , latent heat of vaporization L , global-mean surface air relative humidity \mathcal{H}_0 , specific heat capacity of air c_p , and saturation specific humidity q^* . Here, the radiative forcing, feedback and diffusivity are assumed spatially uniform. PA is larger when (3) is more positive, as the climatological $\overline{T_2}$ is negative (colder pole). For warmer T_0 , the increase in the numerator from $\partial_{TT}q^*|_{\overline{T_0}}$ implies a larger increase in atmospheric energy transport and enhanced PA. For stronger meridional temperature gradients, the increase in the numerator from $-\overline{T_2}$ likewise implies a larger increase in atmospheric energy transport and enhanced PA.

Figure 1b shows the moist EBM has similar dependence on the base climate as the GCM for the selected base states, with less spatial structure and weaker warming at the pole. The PA metric $\widetilde{\text{PA}}$ for the moist EBM theory (3) is shown in Figure 1d. The overall state-dependence is comparable to the GCM results, with somewhat smaller magnitude variation. The GCM includes additional structure in perturbations to its local energy budget compared to the moist EBM theory, which we examine next.

4 Local Energy Budget Analysis

4.1 Method

Many analyses of local energy budgets express results in terms of the local temperature change needed for the Planck feedback to rebalance individual changes that arise from radiative forcing, feedback, or energy transport (with the earliest examples being Winton, 2006; Lu & Cai, 2009; Crook et al., 2011; Feldl & Roe, 2013). This diagnostic approach has the limitation that it cannot elucidate the underlying interactions between local energy budget perturbations (as has been illustrated in both EBM and idealized GCM simulations with perturbed surface albedo formulation, Merlis et al., 2014; Feldl et al., 2017) and it cannot capture the forcing-agent dependence of the lapse-rate feedback of the radiative-advective equilibrium regime of the high-latitude atmosphere (Cronin

& Jansen, 2016; Henry & Merlis, 2020; Caballero & Merlis, 2025). Despite the diagnostic nature of this approach, we evaluate the local energy budget changes, expressed as temperature changes, to shed light on the relative roles of atmospheric energy transport vs. radiative processes in the state-dependence of PA found in this series of simulations. The local temperature change is a function of the radiative forcing \mathcal{F} , local radiative feedbacks λ_i , and divergence of the moist static energy (h) flux:

$$\Delta T_s = \frac{-\mathcal{F} - \Delta(\nabla \cdot \{\mathbf{u}h\}) - \Delta T_s \Sigma_i \lambda_i}{\langle \lambda_P \rangle}, \quad (4)$$

with Planck feedback λ_P , global mean indicated by $\langle \cdot \rangle$, and column integral indicated by $\{\cdot\}$. The sum over feedbacks includes the spatially varying component of the Planck feedback and lapse rate feedback. (In comprehensive GCMs, the feedbacks λ_i would also include the water vapor, cloud, and surface albedo feedback.)

The vertically integrated divergence of meridional atmospheric energy transport is determined from the atmospheric energy budget:

$$\nabla \cdot \{\mathbf{u}h\} = N - Q, \quad (5)$$

with net radiation N and Q-flux Q (i.e., the sum of the surface energy fluxes). Analogously, the vertically integrated divergence of meridional latent energy transport is obtained from the precipitation minus evaporation. The total feedback—here, just the temperature feedback—is calculated using the perturbation TOA budget:

$$\lambda(\phi) = \frac{-\mathcal{F} - \Delta(\nabla \cdot \{\mathbf{u}h\})}{\Delta T_s}. \quad (6)$$

The Planck feedback is calculated by an additional online call to the radiative transfer scheme with the temperature field perturbed by one kelvin (Merlis et al., 2022). This is more straightforward than calculating a radiative kernel for a specific aquaplanet set up, though that can be done (Feldl & Roe, 2013; Chung & Feldl, 2024).

4.2 GCM-Simulated Energy Budget Changes

Figure 2 shows a select number of local energy budget analyses (Eq. 4) for illustrative climate states. For an approximately Earth-like base state ($T_0 = 280$ K, $\Delta_h T = -45$ K, Figure 2a), the pattern of warming is polar amplified (blue line) with about twice as much warming at the pole. The radiative forcing is tropically amplified (orange line) and the other three local energy budget factors have polar amplified structure. They are, in order of smallest-to-largest polar amplified structure: the spatially varying Planck feedback (red), the lapse rate feedback (purple), and the change in the divergence of the atmospheric energy transport (green).

For the same meridional temperature gradient, but a hotter global-mean surface temperature ($T_0 = 300$ K, $\Delta_h T = -45$ K, Figure 2b), there is more polar amplified temperature change (blue line). The individual factors have broadly similar structure in this hot climate, though the forcing, expressed as a temperature change, is flatter and the change in the divergence of the atmospheric energy transport has enhanced changes (that is, contributes more to polar amplification). The temperature feedback components have different ordering at the pole with the spatially varying Planck now larger than the lapse rate feedback. We note that changes in individual energy budget components in the low latitudes also play a role in determining the meridional pattern of warming.

For the same global-mean surface temperature, but a stronger meridional temperature gradient ($T_0 = 280$ K, $\Delta_h T = -90$ K, Figure 2d), there is more polar amplified temperature change (blue line). The individual factors have broadly similar structure in this strong temperature-gradient climate: enhanced meridional contrast is readily apparent in the radiative forcing (orange line, tending toward more tropically amplified warm-

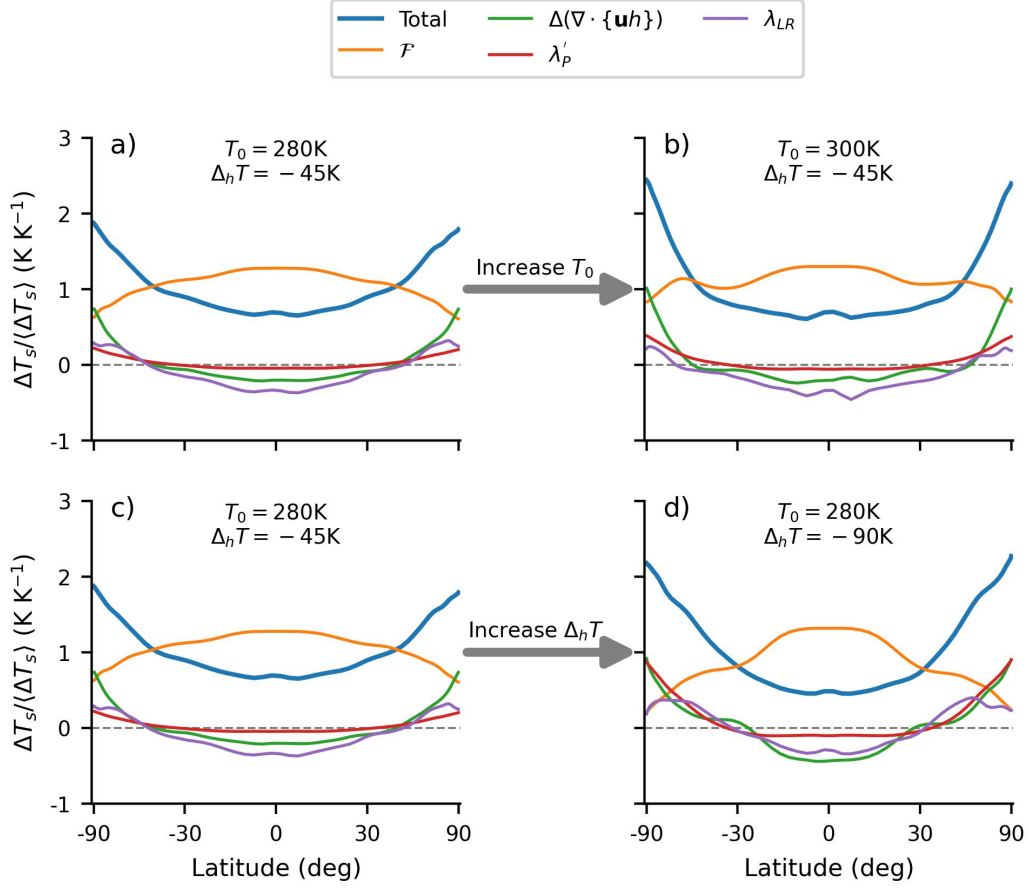


Figure 2. Local energy budget analysis of temperature changes vs. latitude for (a,c) an Earth-like base state ($T_0 = 280\text{ K}$, $\Delta_h T = -45\text{ K}$), (b) a hot global-mean surface temperature base state with unchanged meridional temperature gradients ($T_0 = 300\text{ K}$, $\Delta_h T = -45\text{ K}$), and (d) a strong meridional temperature gradient base state with unchanged global-mean surface temperature ($T_0 = 280\text{ K}$, $\Delta_h T = -90\text{ K}$). The colors correspond to different components as indicated in the legend and described in section 4.1 and Eq. 4.

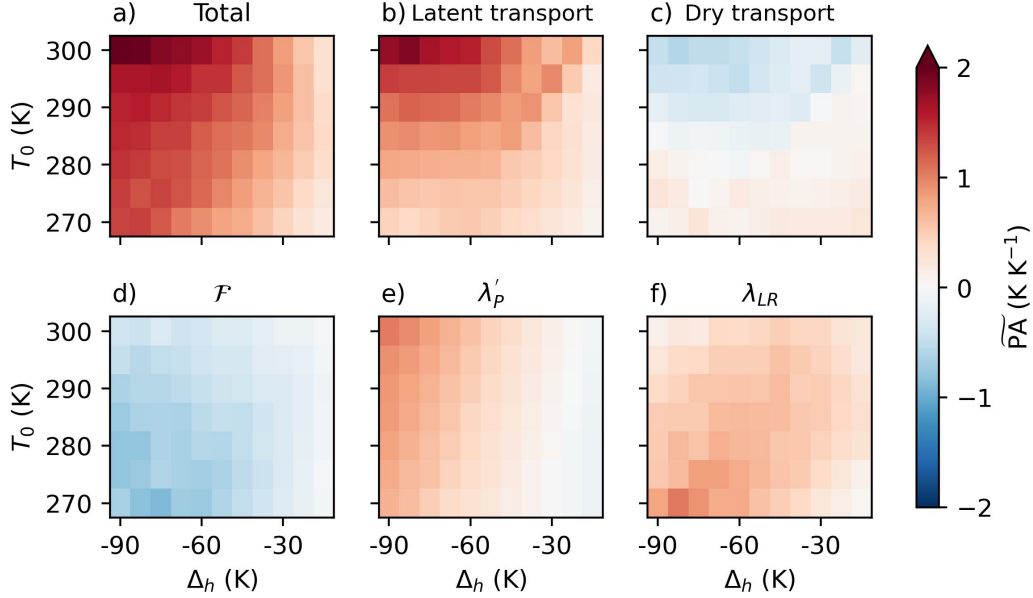


Figure 3. The state-dependence of a PA metric (Eq. 2) (a), and contributions from (b) atmospheric energy transport, (c) latent energy transport, (d) radiative forcing, (e) spatially varying Planck feedback, and (f) lapse rate feedback.

ing), the spatially varying Planck feedback (red line, tending toward more polar amplified warming), and atmospheric energy transport (green line, tending toward more polar amplified warming). The atmospheric energy transport term has modest changes in high-latitudes, but there is a state-dependence arising from its larger increase in divergence out of low latitudes—i.e., more tropical cooling in the stronger temperature gradient base climate. There are also changes in the lapse rate feedback, though these are largest in the midlatitudes. We next systematically evaluate these energy budget changes over the range of climates.

Figure 3 shows the results of the local energy budget analysis (Eq. 4), where each panel has a normalized horizontal temperature contrast metric \widetilde{PA} from one of the right-hand side terms of Eq. 4. This metric is positive if the local energy budget component contributes to more high-latitude warming (red in Fig. 3) and is negative if the local energy budget component contributes to more low-latitude warming (blue in Fig. 3). Figure 3a reproduces the total change of Fig. 1c.

Breaking down the individual components of the local energy budget analysis, we see that the latent component of the energy transport has the largest state-dependence and captures much of the total state-dependence of \widetilde{PA} (Fig. 3b). However, the dry component of the moist static energy transport has a countervailing influence, though with smaller magnitude (Fig. 3c). This implies the combined energy transport does not fully account for the state-dependence of PA, leaving a role for radiative processes. The isolated effect of spatially varying radiative forcing tends toward tropically amplified warming, and this is somewhat more pronounced in cold global-mean and strong temperature gradient climates (Fig. 3d). The spatially varying component of the Planck feedback has a similar sense to the overall state-dependence, with a larger role for strong temperature gradient and warm climates (Fig. 3e). Last, the lapse rate feedback has state-dependence that promotes PA in intermediate (in both global mean and gradients) climates and in cold climates with strong meridional temperature gradients (Fig. 3f).

The radiative forcing and Planck feedback have a substantial amount of shared, counteracting state-dependence. This arises from their common dependence on the control climate’s emission temperature. The outgoing longwave radiation perturbation from a unit of warming is $\approx (4\sigma\bar{T}_{em}^3) \times 1 \text{ K}$, with emission temperature T_{em} . The outgoing longwave radiation perturbation from radiative forcing is $\approx (4\sigma\bar{T}_{em}^3) \times \delta p_{em} \partial_T p_{em}$, with emission pressure p_{em} and its changes are negative as the additional longwave absorber shifts the emission to lower pressure. It is clear that the dependence on the third power of the climatological emission temperature cancels between these two radiative flux components, while the extent to which the temperature shift in emission ($\delta p_{em} \partial_T p_{em}$) is close to 1 K can vary across the climate states. Combining these two factors (Fig. S1) does leave a modest state-dependence that contributes to the aggregate PA state-dependence.

In summary, atmospheric energy transport plays the dominant role in the state-dependence of PA in this wide range of climates. There is a role for radiative processes, with a net contribution of the feedbacks and forcing pushing toward similar state-dependence.

5 Conclusion

Polar amplification is a ubiquitous aspect of simulations of climate change, though most of these are perturbations about Earth’s present-day climate. Examining the state-dependence of polar amplification was motivated by (i) the role that atmospheric energy transport, particularly latent energy transport, is known to play in PA (e.g., Solomon, 2006) and (ii) the dependence of scaling theories for atmospheric energy transport on climatological temperature and temperature gradients (Caballero & Langen, 2005). These state-dependent energy transport dynamics are encapsulated in down-gradient moist static energy diffusion and, therefore, diffusive moist EBMs have state-dependent PA (Merlis & Henry, 2018, Fig. 1d).

Here, we presented the first systematic examination of the state-dependence of PA in GCM simulations of warming, using an idealized, ice-free aquaplanet GCM. The simulations show that PA is state-dependent, with warmer global-mean surface temperature control climates having more PA and stronger equator-to-pole temperature gradient climates having more PA. This overall behavior is qualitatively consistent with expectations from moist EBM theory (Eq. 3) where state-dependence is driven by enhanced down-gradient diffusion of moist static energy in climates with stronger climatological moist static energy gradients. Our GCM simulations exhibit a similar state-dependence of changes in latent energy transport (Fig. 3b), but the GCM has additional pathways to PA which are not present in the moist EBM.

We note that the moist EBM theory used here assumes atmospheric energy transport can be modeled as down-gradient diffusion with a diffusivity, \mathcal{D} , which does not change with warming. To test this assumption, we used the optimization procedure of Lu et al. (2022) to calculate a latitudinally-resolved diffusivity, and found that fractional changes in globally-averaged \mathcal{D} with warming are relatively small across the range of climates considered (Fig. S2).

The spatial structure of the temperature feedback has been identified as an important factor in PA in comprehensive GCMs and the idealized GCM has both the Planck feedback (less stabilizing feedback in high latitudes because of climatologically colder temperatures) and lapse rate feedback, with a stabilizing feedback parameter in low latitudes and a destabilizing feedback parameter in high latitudes, that promotes PA. While these have previously been quantified for an Earth-like control state, their state-dependence had not been assessed. Here, we found that they have some state-dependence, with the Planck feedback contributing to the overall behavior of warmer and/or strong gradient climates having more PA and the lapse rate playing a substantial role in cold, strong gra-

dient climates. However, this was sub-dominant to the state-dependence of energy transport.

The local energy budget analysis (Fig. 3) uses a conventional decomposition for radiative feedbacks that is inspired by climate sensitivity research. There and in the local budget assessed here, it is natural to ask what terms are physically connected and should be combined. The spatial structure of the radiative forcing and Planck feedback are connected because they both involve perturbations to the emission temperature. The combined effect of these spatially varying components of the energy budget contributes to the overall state-dependence of PA.

The atmospheric energy transport is also connected to the local, high-latitude lapse rate feedback (Cronin & Jansen, 2016; Feldl et al., 2020). In particular, the dry component of the energy transport is connected to the mid- and upper-troposphere via isentropic advection, promoting a more vertically uniform atmospheric temperature change in high-latitudes than the lapse rate change from greenhouse gas or surface flux perturbation, which have more bottom heavy lapse rate change. In contrast, the low latitude lapse rate feedback is primarily controlled locally by moist adiabatic temperature change. A close analysis of the zonal-mean structure of temperature change in this set of simulations would be a valuable step toward understanding the state-dependence of its contribution to PA.

The idealized GCM simulations presented here omit important processes for PA, including those related to sea ice. Sea ice, naturally, introduces additional state-dependence because the freezing point is an absolute temperature threshold of the climate system. So, its role in PA deactivates in sufficiently hot climates. There are also nonlinearities in cold climate states: the threshold for the snowball Earth, large ice-cap instability creates a major state-dependence for the spatial structure of temperature change. Beyond these extremes, intermediate climate states may also exhibit state-dependence (Kay et al., 2024). Quantifying the relative roles of ice processes in PA state-dependence compared to the atmospheric energy transport mechanism shown to dominate the idealized climates considered here is a fruitful avenue for future research.

Open Research Section

The Isca model is available on GitHub (github.com/ExeClim/Isca); simulations were conducted using commit 5c6d5ba. A Zenodo repository with analysis code to reproduce the figures is available at Williams (2025).

Acknowledgments

A.I.L. Williams acknowledges funding from the CIMES Postdoctoral Fellowship under award NA18OAR4320123 from the National Oceanic and Atmospheric Administration, U.S. Department of Commerce. This research was supported in part by grant NSF PHY-2309135 to the Kavli Institute for Theoretical Physics (KITP).

The simulations presented in this paper were performed using High Performance Computing resources provided by the Cooperative Institute for Modeling the Earth System.

We are grateful to Neil Lewis, Stephen Thomson, and Tra Dinh for technical assistance with configuring and running Isca. We thank Lily Hahn, Rodrigo Caballero, and Nicole Feldl for scientific feedback, and Sampson Schamerhorn for encouragement.

References

- Bonan, D. B., Armour, K. C., Roe, G. H., Siler, N., & Feldl, N. (2018). Sources of uncertainty in the meridional pattern of climate change. *Geophys. Res. Lett.*, *45*, 9131–9140.
- Caballero, R., & Langen, P. L. (2005). The dynamic range of poleward energy transport in an atmospheric general circulation model. *Geophys. Res. Lett.*, *32*, L02705. (doi:10.1029/2004GL021581)
- Caballero, R., & Merlis, T. M. (2025). Polar feedbacks in clearsky radiative-advective equilibrium from an air-mass transformation perspective. *Journal of Climate*. doi: <https://doi.org/10.1175/JCLI-D-24-0031.1>
- Chang, C.-Y., & Merlis, T. M. (2023). The role of diffusivity changes on the pattern of warming in energy balance models. *J. Climate*, *36*, 7993–8006.
- Chung, P.-C., & Feldl, N. (2024). Sea ice loss, water vapor increases, and their interactions with atmospheric energy transport in driving seasonal polar amplification. *J. Climate*, *37*, 2713–2725.
- Cronin, T. W., & Jansen, M. F. (2016). Analytic radiative-advective equilibrium as a model for high-latitude climate. *Geophys. Res. Lett.*, *43*, 449–457.
- Crook, J. A., Forster, P. M., & Stuber, N. (2011). Spatial patterns of modeled climate feedback and contributions to temperature response and polar amplification. *J. Climate*, *24*, 3575–3592.
- Feldl, N., Bordoni, S., & Merlis, T. M. (2017). Coupled high-latitude climate feedbacks and their impact on atmospheric heat transport. *J. Climate*, *30*, 189–201.
- Feldl, N., & Merlis, T. M. (2021). Polar amplification in idealized climates: the role of ice, moisture, and seasons. *Geophys. Res. Lett.*, *48*, e2021GL094130.
- Feldl, N., Po-Chedley, S., Singh, H. K. A., Hay, S., & Kushner, P. J. (2020). Sea ice and atmospheric circulation shape the high-latitude lapse rate feedback. *npj Clim. Atmos. Sci.*, *3*, 1–9.
- Feldl, N., & Roe, G. H. (2013). The nonlinear and nonlocal nature of climate feedbacks. *J. Climate*, *26*, 8289–8304.
- Flannery, B. P. (1984). Energy balance models incorporating transport of thermal and latent energy. *J. Atmos. Sci.*, *41*, 414–421.
- Frierson, D. M. W. (2007). The dynamics of idealized convection schemes and their effect on the zonally averaged tropical circulation. *J. Atmos. Sci.*, *64*, 1959–1976.
- Frierson, D. M. W., Held, I. M., & Zurita-Gotor, P. (2006). A gray-radiation aquaplanet moist GCM. Part I: Static stability and eddy scale. *J. Atmos. Sci.*, *63*, 2548–2566.
- Guendelman, I., & Kaspi, Y. (2020). Atmospheric dynamics on terrestrial planets with eccentric orbits. *Astrophys. J.*, *901*, 46.
- Hahn, L. C., Armour, K. C., Battisti, D. S., Donohoe, A., & Fajber, R. (2023). Seasonal changes in atmospheric heat transport to the Arctic under increased CO_2 . *Geophys. Res. Lett.*, *50*, e2023GL105156.
- Hahn, L. C., Armour, K. C., Zelinka, M. D., Bitz, C. M., & Donohoe, A. (2021). Contributions to polar amplification in CMIP5 and CMIP6 models. *Frontiers in Earth Science*, *9*, 710036.
- Held, I. M., Delworth, T. L., Lu, J., Findell, K. L., & Knutson, T. R. (2005). Simulation of Sahel drought in the 20th and 21st centuries. *Proc. Nat. Acad. Sci.*, *102*, 17891–17896.
- Henry, M., & Merlis, T. M. (2019). The role of the nonlinearity of the Stefan-Boltzmann law on the structure of radiatively forced temperature change. *J. Climate*, *32*, 335–348.
- Henry, M., & Merlis, T. M. (2020). Lapse rate changes dominate residual polar warming in solar radiation management experiments. *Geophys. Res. Lett.*, *47*, e2020GL087929.

- Henry, M., & Vallis, G. K. (2022). Variations on a pathway to an early Eocene climate. *Paleoceanogr. Paleoclimatol.*, *37*, e2021PA004375.
- Hill, S. A., Burls, N. J., Fedorov, A., & Merlis, T. M. (2022). Symmetric and antisymmetric components of polar-amplified warming. *J. Climate*, *35*, 3157–3172.
- Huber, M., & Caballero, R. (2011). The early Eocene equable climate problem revisited. *Clim. Past*, *7*, 603–633.
- Hwang, Y.-T., Frierson, D. M. W., & Kay, J. E. (2011). Coupling between Arctic feedbacks and changes in poleward energy transport. *Geophys. Res. Lett.*, *38*, L17704.
- Jeevanjee, N., Hassanzadeh, P., Hill, S., & Sheshadri, A. (2017). A perspective on climate model hierarchies. *J. Adv. Model. Earth Syst.*, 1760–1771.
- Kaspi, Y., & Showman, A. P. (2015). Atmospheric dynamics of terrestrial exoplanets over a wide range of orbital and atmospheric parameters. *Astrophys. J.*, *804*, 60.
- Kay, J. E., Liang, Y.-C., Zhou, S.-N., & Maher, N. (2024). Sea ice feedbacks cause more greenhouse cooling than greenhouse warming at high northern latitudes on multi-century timescales. *Environmental Research: Climate*, *3*, 041003.
- Kluft, L., Dacie, S., Buehler, S. A., Schmidt, H., & Stevens, B. (2019). Re-examining the first climate models: Climate sensitivity of a modern radiative-convective equilibrium model. *J. Climate*, *32*, 8111–8125.
- Langen, P. L., Graversen, R. G., & Mauritsen, T. (2012). Separation of contributions from radiative feedbacks to polar amplification on an aquaplanet. *J. Climate*, *25*, 3010–3024.
- Lu, J., & Cai, M. (2009). A new framework for isolating individual feedback processes in coupled general circulation climate models. Part I: Formulation. *Clim. Dyn.*, *32*, 873–885.
- Lu, J., Zhou, W., Kong, H., Leung, L. R., Harrop, B., & Song, F. (2022). On the diffusivity of moist static energy and implications for the polar amplification response to climate warming. *J. Climate*, *35*, 3521–3540.
- Maher, P., Gerber, E. P., Medeiros, B., Merlis, T. M., Sherwood, S., Sheshadri, A., ... Zurita-Gotor, P. (2019). Model hierarchies for understanding atmospheric circulation. *Rev. Geophys.*, *57*, 250–280.
- Manners, J., et al. (2017). *Socrates technical guide: Suite of community radiative transfer codes based on edwards and slingo* (Tech. Rep.). Technical Report, Met Office, Exeter, UK.
- Masson-Delmotte, V., Kageyama, M., Braconnot, P., Charbit, S., Krinner, G., Ritz, C., ... others (2006). Past and future polar amplification of climate change: climate model intercomparisons and ice-core constraints. *Clim. Dyn.*, *26*, 513–529.
- Merlis, T. M., Feldl, N., & Caballero, R. (2022). Changes in poleward atmospheric energy transport over a wide range of climates: Energetic and diffusive perspectives and a priori theories. *J. Climate*, *35*, 2933–2948.
- Merlis, T. M., Held, I. M., Stenchikov, G. L., Zeng, F., & Horowitz, L. (2014). Constraining transient climate sensitivity using coupled climate model simulations of volcanic eruptions. *J. Climate*, *27*, 7781–7795.
- Merlis, T. M., & Henry, M. (2018). Simple estimates of polar amplification in moist diffusive energy balance models. *J. Climate*, *31*, 5811–5824.
- Mlawer, E. J., Taubman, S. J., Brown, P. D., Iacono, M. J., & Clough, S. A. (1997). Radiative transfer for inhomogeneous atmospheres: RRTM, a validated correlated-k model for the longwave. *J. Geophys. Res.*, *102*, 16663–16682.
- O’Gorman, P. A., & Schneider, T. (2008a). Energy of midlatitude transient eddies in idealized simulations of changed climates. *J. Climate*, *21*, 5797–5806.
- O’Gorman, P. A., & Schneider, T. (2008b). The hydrological cycle over a wide range of climates simulated with an idealized GCM. *J. Climate*, *21*, 3815–3832.

- Solomon, A. (2006). Impact of latent heat release on polar climate. *Geophys. Res. Lett.*, *33*, L07716.
- Taylor, P. C., Boeke, R. C., Boisvert, L. N., Feldl, N., Henry, M., Huang, Y., ... Tan, I. (2022). Process drivers, inter-model spread, and the path forward: A review of amplified Arctic warming. *Frontiers in Earth Science*, *9*.
- Vallis, G. K., Colyer, G., Geen, R., Gerber, E., Jucker, M., Maher, P., ... Thomson, S. I. (2018). Isca, v1.0: A framework for the global modelling of the atmospheres of earth and other planets at varying levels of complexity. *Geosci. Model Dev.*, *11*, 843–859.
- Williams, A. I. L. (2025). Supporting data for “state-dependence of polar amplification in an idealized, ice-free gcm”. [dataset]. *Zenodo*. doi: 10.5281/zenodo.15830418
- Winton, M. (2006). Amplified Arctic climate change: What does surface albedo feedback have to do with it? *Geophys. Res. Lett.*, *33*, L03701.